Supporting Information:

Numerical analysis of Homojunction design for high-efficiency Pb-free Perovskite Solar Cells

*Bita Farhadi[1], Yufei Shao[2], Dan Yang[2], Kai Wang[2, *], Shengzhong Liu[2, 3, *]*

[1] EIT Data Science and Communication College, Zhejiang Yuexiu University, Shaoxing, China

[2] Key Laboratory of Photoelectric Conversion and Utilization of Solar Energy, Center of Materials Science and Optoelectronics Engineering, Dalian Institute of Chemical Physics, University of Chinese Academy of Sciences, Chinese Academy of Sciences, Dalian 116023, China.

[3] China National Nuclear Power Co., Ltd. Beijing, 100089, China

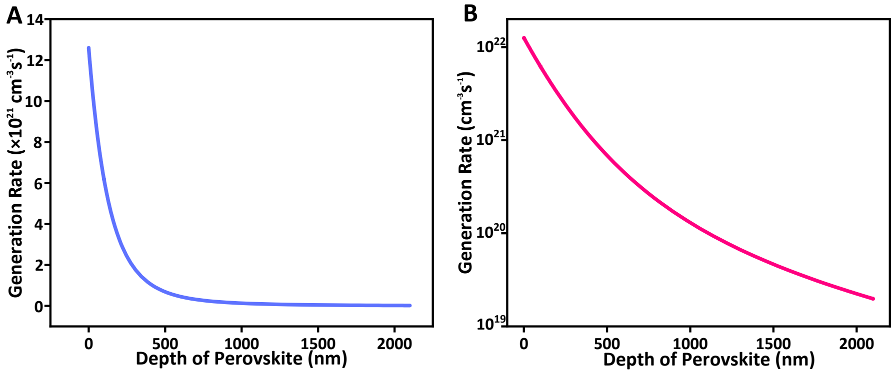

Figure S1. A) The carrier generation rate profile and, B) The associated exponential representation.

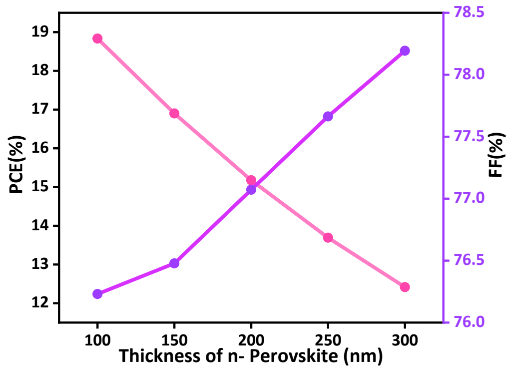

Figure S2. The variations in FF and PCE with respect to changes in d_n, while d_p remains fixed at 2000 nm.

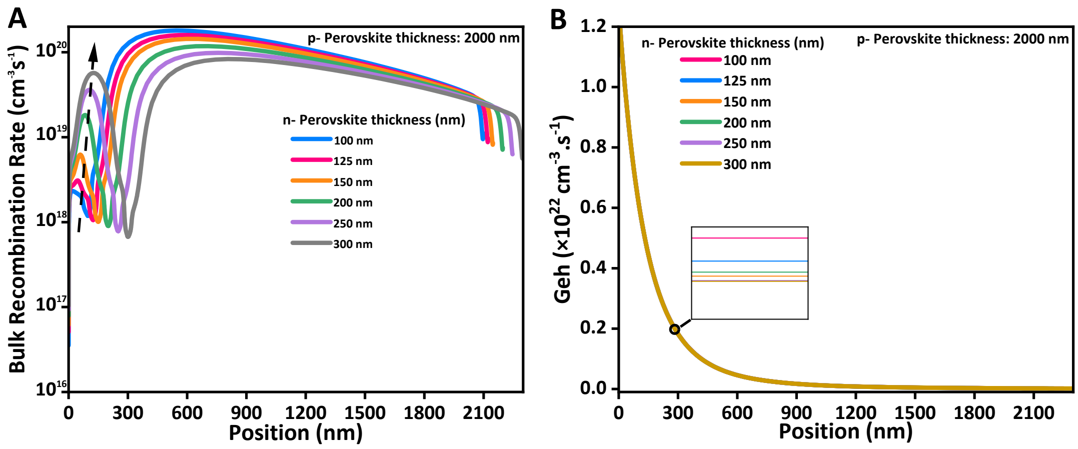

Figure S3. A) Bulk recombination rate distributions for various thickness values of n-perovskite, B) Direct band-to-band excitation of electron-hole pairs for various thickness values of n-perovskite.

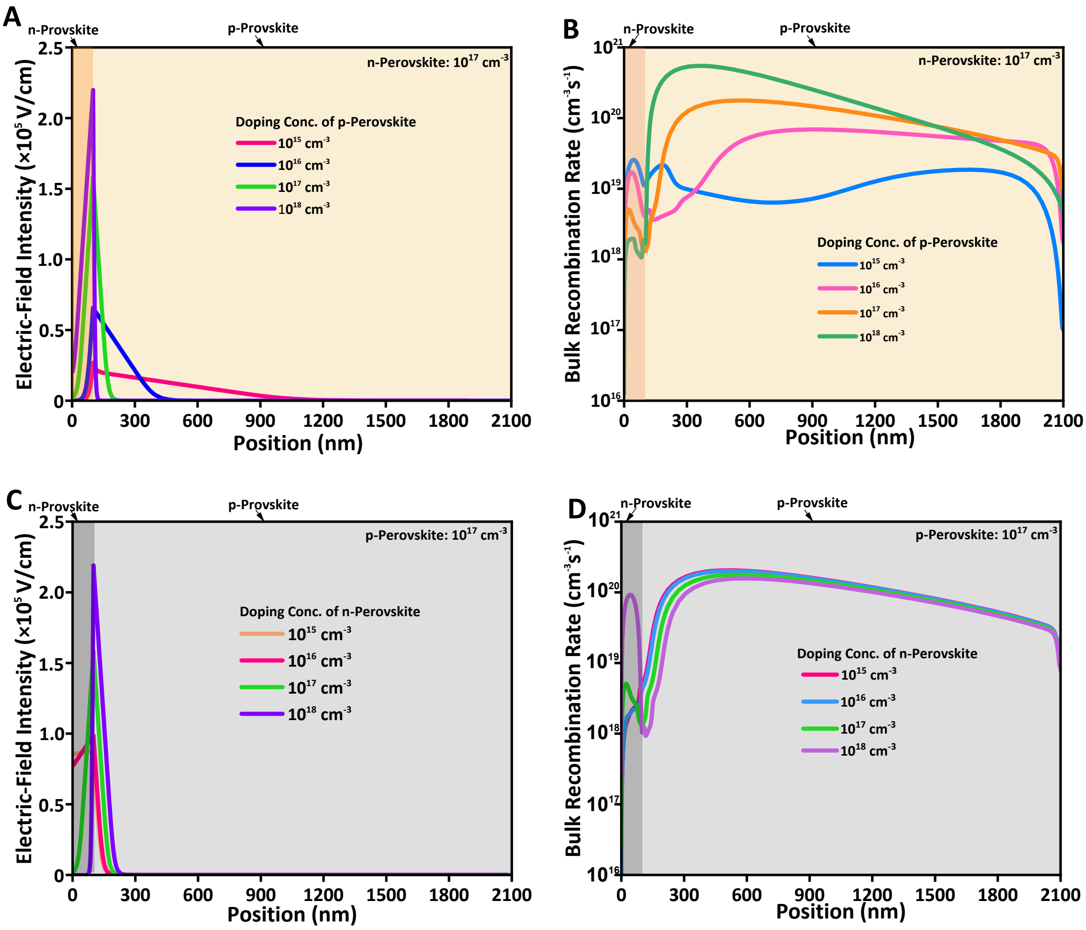

Figure S4. (A, C) electric-field intensity distributions and (B, D) bulk recombination rate distributions for four representative values of n- Perovskite or p- Perovskite, specifically 10^{15},10^{16},10^{17} and 10^{18} cm^{-3}.

Table S1- Initial Input Parameters for HTLs, $FA_{0.75}MA_{0.25}Sn_{0.95}Ge_{0.05}I_3$ and $MAPbI_3$ absorber layers.

Parameters	PTAA [1]	Spiro-MeOTAD [2, 3]	P3HT [3]	$SrCu_2O_2$ [4, 5]	CuSCN [3]	$CuCrO_2$ [6]	$FA_{0.75}MA_{0.25}Sn_{0.95}Ge_{0.05}I_3$ [7]	$MAPbI_3$ [2]
Thickness (nm)	30	150	50	150	50	50	100-1000	100-1000
Band gap, E_g (eV)	2.96	2.70	1.70	3.30	3.60	3	1.40	1.57
Electron affinity, X (eV)	2.30	2.50	3	2.20	1.70	2.10	3.67	3.90
Dielectric permittivity (relative), ε_r	9	3	3.50	9.77	10	9.50	8.20	6.50
CB effective density of states, N_C (1/cm^3)	1×10^{21}	2.2×10^{18}	2×10^{21}	2.2×10^{18}	2.2×10^{19}	1×10^{19}	2.2×10^{18}	2.2×10^{18}
VB effective density of states, N_V (1/cm^3)	1.8×10^{21}	1.8×10^{19}	2×10^{21}	1.8×10^{19}	1.8×10^{18}	1×10^{19}	1.8×10^{19}	1×10^{19}
Electron mobility, μ_n (cm^2/Vs)	40	2×10^{-4}	1.8×10^{-3}	0.10	100	0.10	2	12.50
Hole mobility, μ_p (cm^2/Vs)	1	2×10^{-4}	1.82×10^{-2}	0.46	25	2.53	2	7.50
Shallow uniform acceptor density, N_A (1/cm^3)	1×10^{18}	1×10^{18}	1×10^{18}	3.6×10^{18}	1×10^{18}	6.4×10^{15}	1×10^{17}	1×10^{17}
Shallow uniform donor density, N_D (1/cm^3)	--	--	--	--	--	--	1×10^{13}	4×10^{15}
Defect density, N_t (1/cm^3)	1×10^{14}	1×10^{14}	1×10^{15}	1×10^{15}	1×10^{15}	1×10^{14}	1×10^{15}	1×10^{15}

Table S2- Initial Input Parameters for ETLs [3, 4, 8-12].

Parameters	WO_3	ZnOS	CdZnS	ZnSe	CdS	TiO_2	IGZO
Thickness (nm)	20	150	60	20	30	30	30
Band gap, E_g (eV)	2.60	2.83	3.18	2.81	2.40	3.20	3.50
Electron affinity, X (eV)	3.80	3.60	3.71	4.09	4.18	4	4.16
Dielectric permittivity (relative), ε_r	13.60	9	10	8.60	10	9	10
CB effective density of states, N_C (1/cm^3)	2.2×10^{17}	2.2×10^{18}	2.5×10^{18}	2.2×10^{18}	2.2×10^{18}	2×10^{18}	5×10^{18}
VB effective density of states, N_V (1/cm^3)	2.2×10^{16}	1.8×10^{19}	2.5×10^{19}	1.9×10^{19}	1.9×10^{19}	1.8×10^{19}	5×10^{18}
Electron mobility, μ_n (cm^2/Vs)	100	100	340	400	100	20	15
Hole mobility, μ_p (cm^2/Vs)	100	25	50	110	50	10	0.1
Shallow uniform acceptor density, N_A (1/cm^3)	--	--	--	--	--	--	--
Shallow uniform donor density, N_D (1/cm^3)	1×10^{18}	1×10^{19}	1×10^{21}	1×10^{21}	1×10^{18}	9×10^{16}	1×10^{17}
Defect density, N_t (1/cm^3)	1×10^{15}	1×10^{15}	1×10^{14}	1×10^{14}	1×10^{15}	1×10^{15}	1×10^{15}

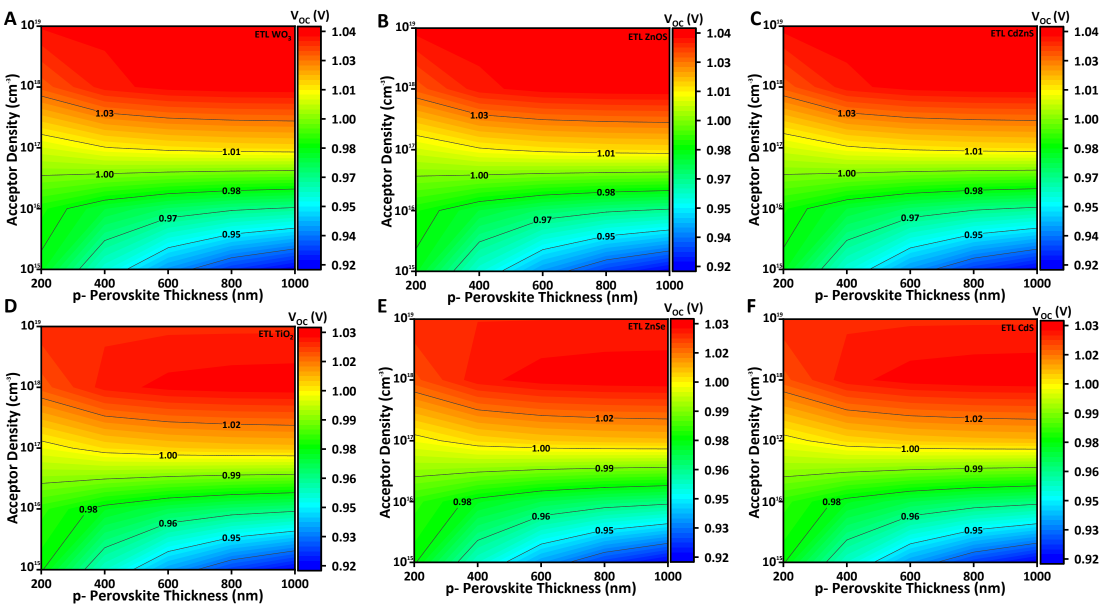

Figure S5. Contour plots demonstrate the simultaneous influence of varying absorber layer thickness and N_A on V_{OC} for $FA_{0.75}MA_{0.25}Sn_{0.95}Ge_{0.05}I_3$-based PSCs when employing different ETLs; A) WO_3, B) ZnOS, C) CdZnS, D) TiO_2, E) ZnSe, and F) CdS.

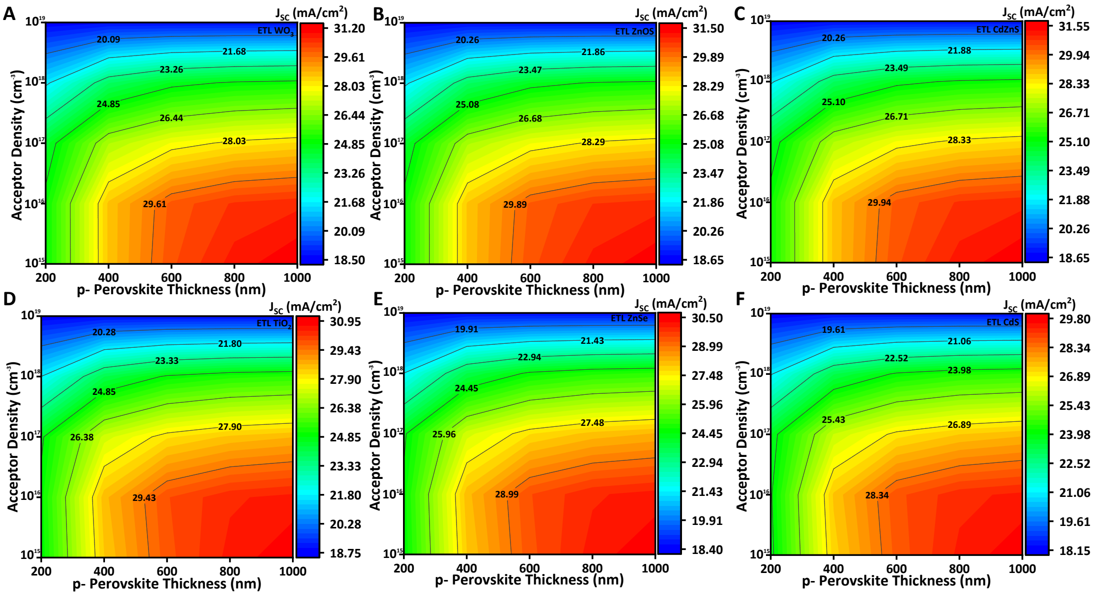

Figure S6. Contour plots demonstrate the simultaneous influence of varying absorber layer thickness and N_A on J_{SC} for $FA_{0.75}MA_{0.25}Sn_{0.95}Ge_{0.05}I_3$-based PSCs when employing different ETLs; A) WO_3, B) ZnOS, C) CdZnS, D) TiO_2, E) ZnSe, and F) CdS.

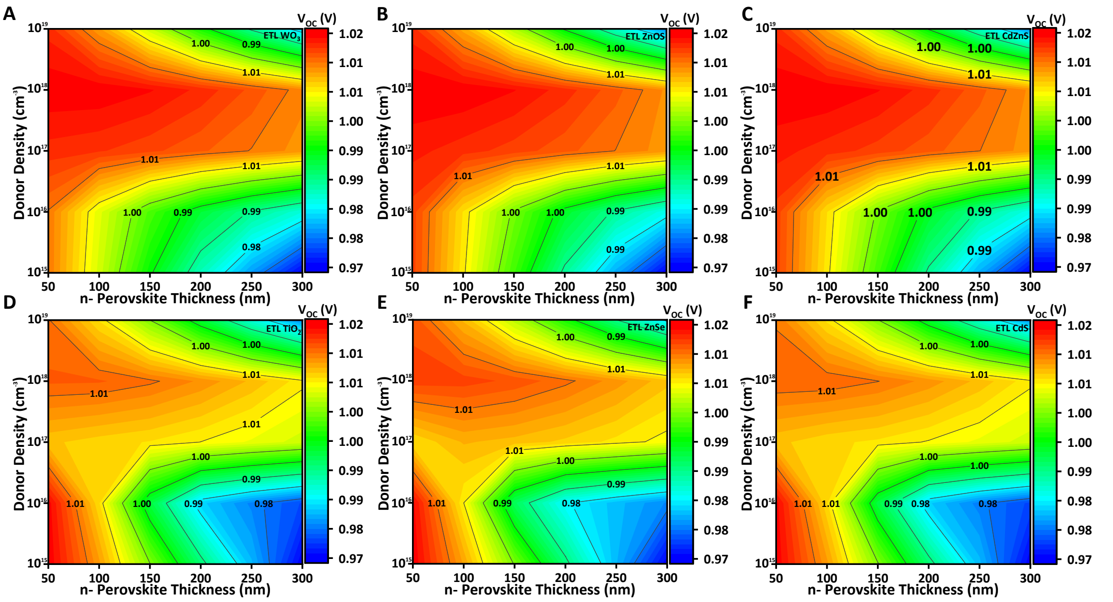

Figure S7. Contour plots demonstrate the simultaneous influence of varying n- perovskite thickness and N_D on V_{OC} for $FA_{0.75}MA_{0.25}Sn_{0.95}Ge_{0.05}I_3$-based PSCs when employing different ETLs; A) WO_3, B) ZnOS, C) CdZnS, D) TiO_2, E) ZnSe, and F) CdS.

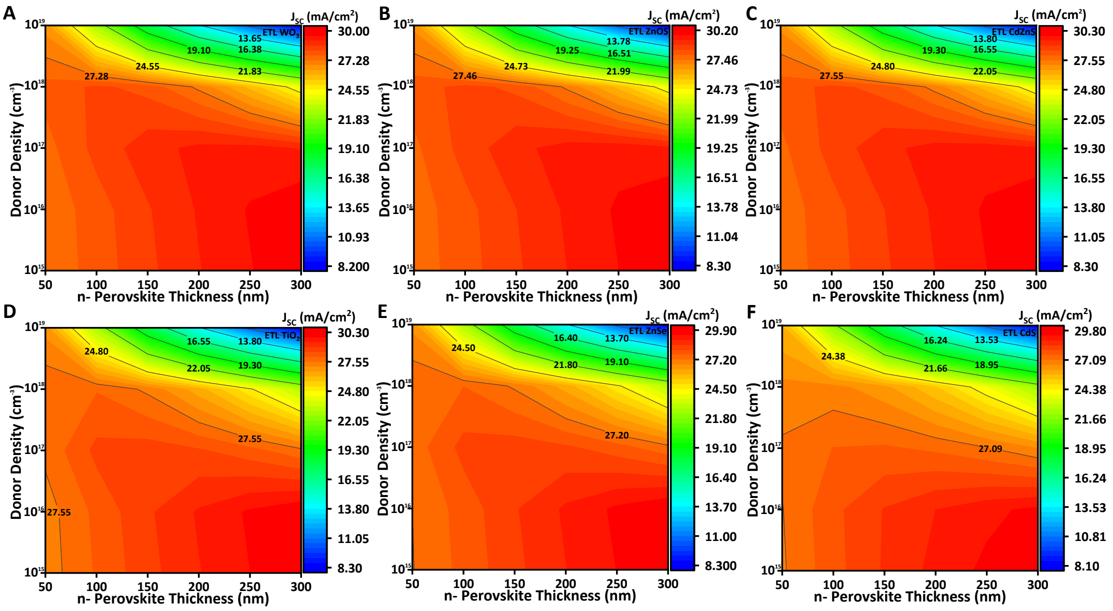

Figure S8. Contour plots demonstrate the simultaneous influence of varying n- perovskite thickness and N_D on J_{SC} for $FA_{0.75}MA_{0.25}Sn_{0.95}Ge_{0.05}I_3$-based PSCs when employing different ETLs; A) WO_3, B) ZnOS, C) CdZnS, D) TiO_2, E) ZnSe, and F) CdS.

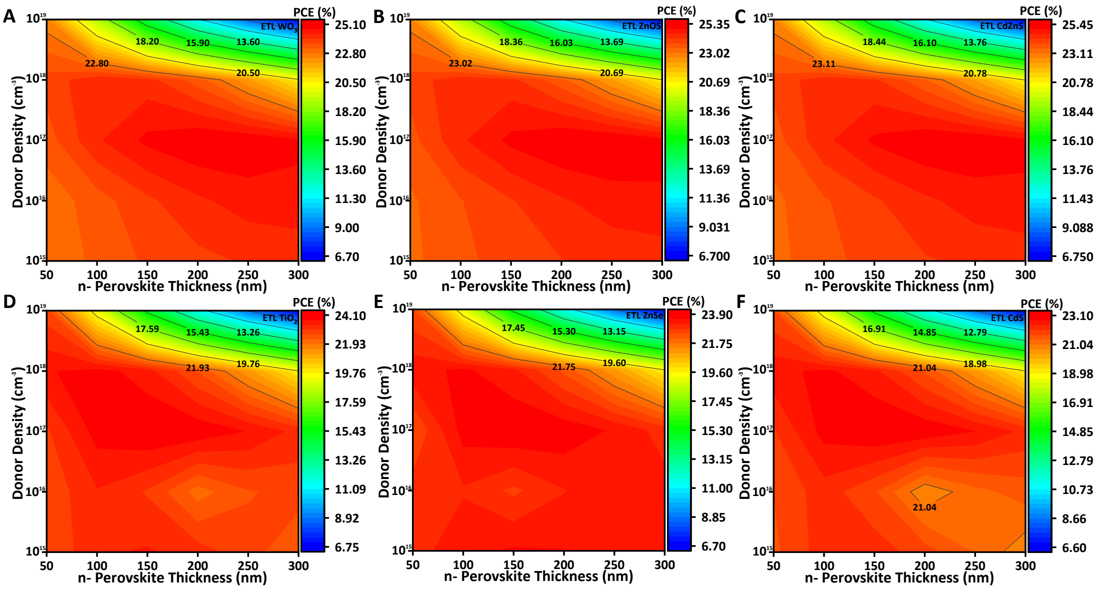

Figure S9. Contour plots demonstrate the simultaneous influence of varying n- perovskite thickness and N_D on PCE for $FA_{0.75}MA_{0.25}Sn_{0.95}Ge_{0.05}I_3$-based PSCs when employing different ETLs; A) WO_3, B) ZnOS, C) CdZnS, D) TiO_2, E) ZnSe, and F) CdS.

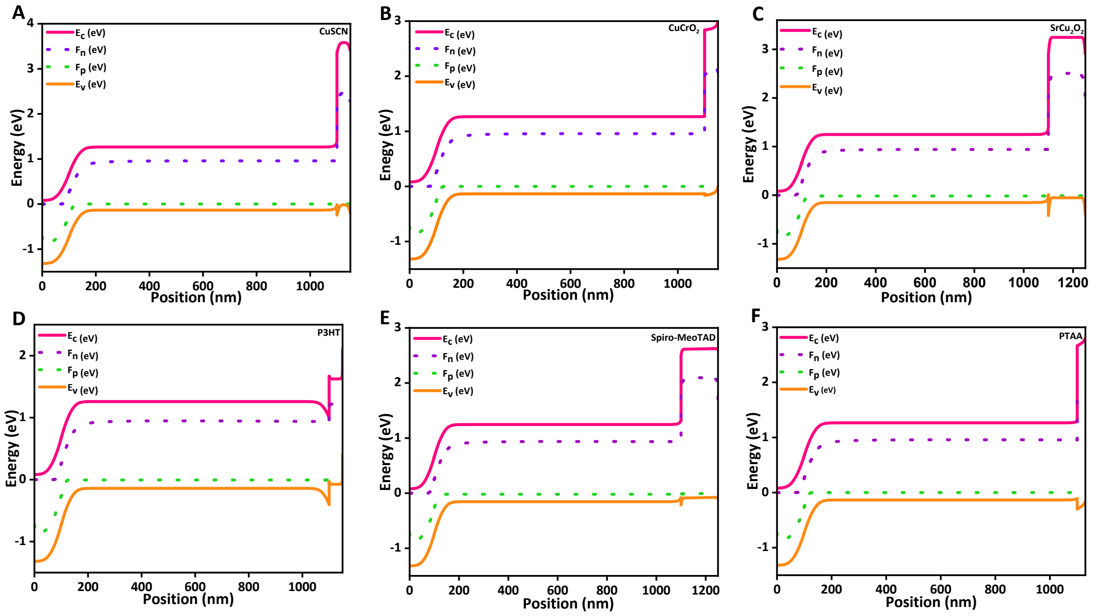

Figure S10. The energy band diagram for $FA_{0.75}MA_{0.25}Sn_{0.95}Ge_{0.05}I_3$-based PSCs when employing different HTLs; A) $CuCrO_2$, B) CuSCN, C) $SrCu_2O_2$, D) P3HT, E) Spiro-MeOTAD, and F) PTAA.

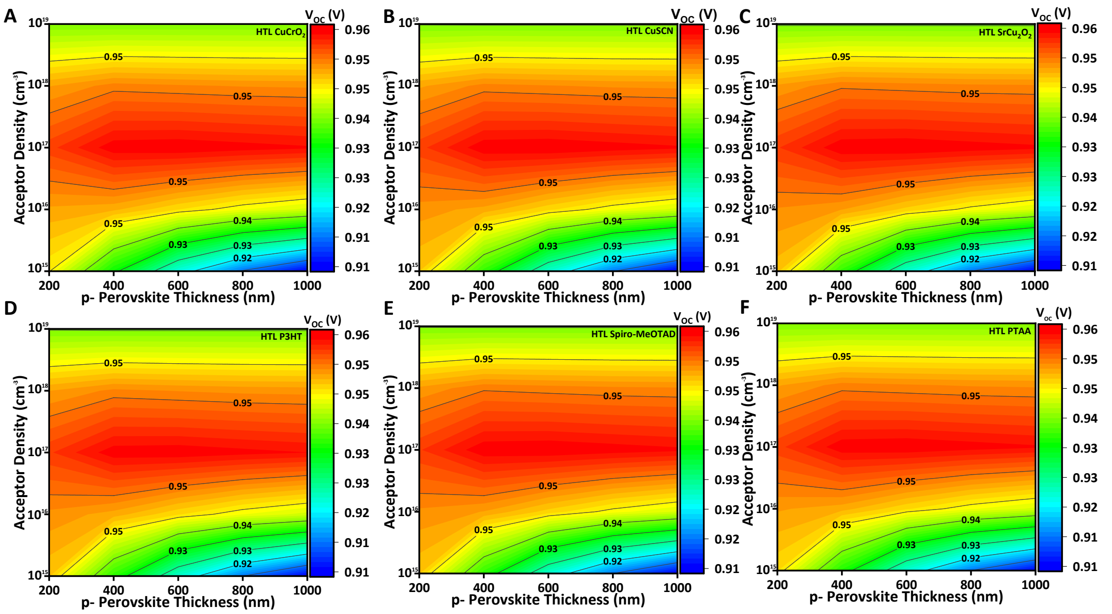

Figure S11. Contour plots demonstrate the simultaneous influence of p- perovskite layer thickness and N_A on V_{OC} for $FA_{0.75}MA_{0.25}Sn_{0.95}Ge_{0.05}I_3$-based PSCs when employing different HTLs; A) $CuCrO_2$, B) CuSCN, C) $SrCu_2O_2$, D) P3HT, E) Spiro-MeOTAD, and F) PTAA.

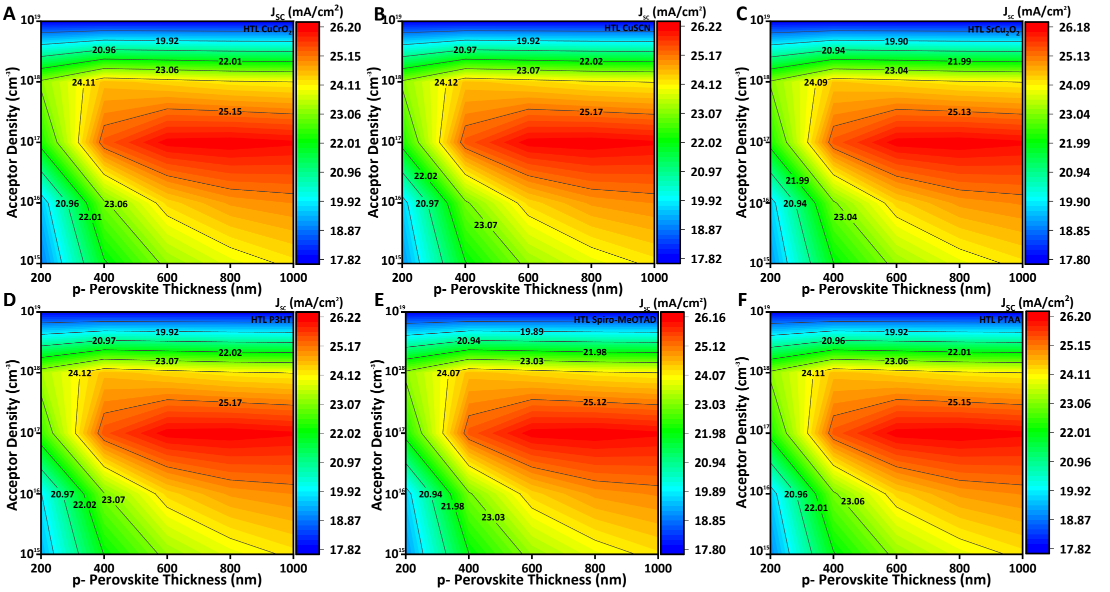

Figure S12. Contour plots demonstrate the simultaneous influence of p- perovskite layer thickness and N_A on J_{SC} for $FA_{0.75}MA_{0.25}Sn_{0.95}Ge_{0.05}I_3$-based PSCs when employing different HTLs; A) $CuCrO_2$, B) CuSCN, C) $SrCu_2O_2$, D) P3HT, E) Spiro-MeOTAD, and F) PTAA.

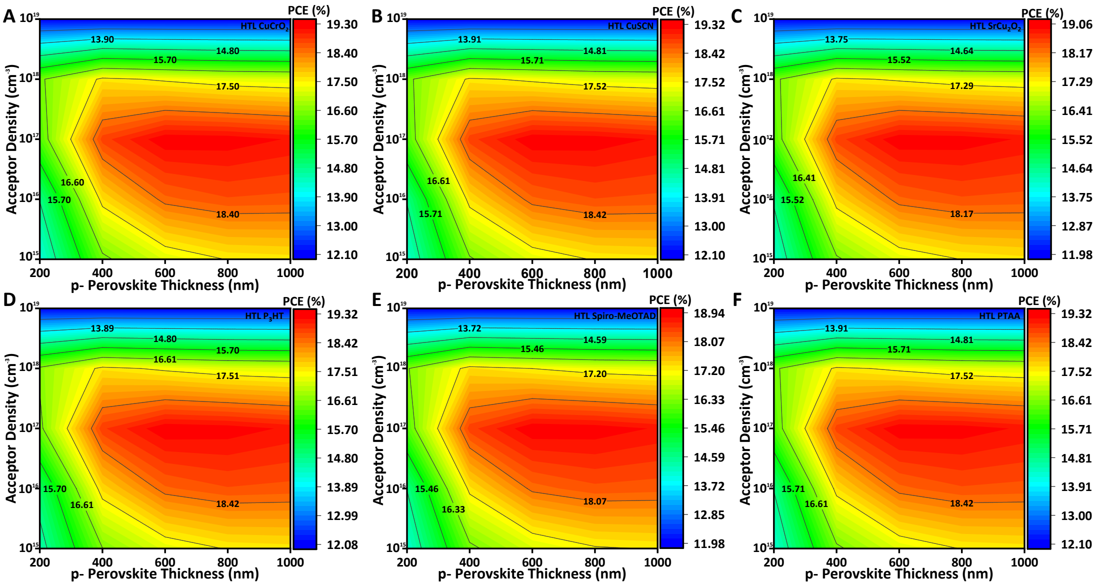

Figure S13. Contour plots demonstrate the simultaneous influence of varying p- perovskite thickness and N_A on PCE for $FA_{0.75}MA_{0.25}Sn_{0.95}Ge_{0.05}I_3$-based PSCs when employing different HTLs; A) $CuCrO_2$, B) CuSCN, C) $SrCu_2O_2$, D) P3HT, E) Spiro-MeOTAD, and F) PTAA.

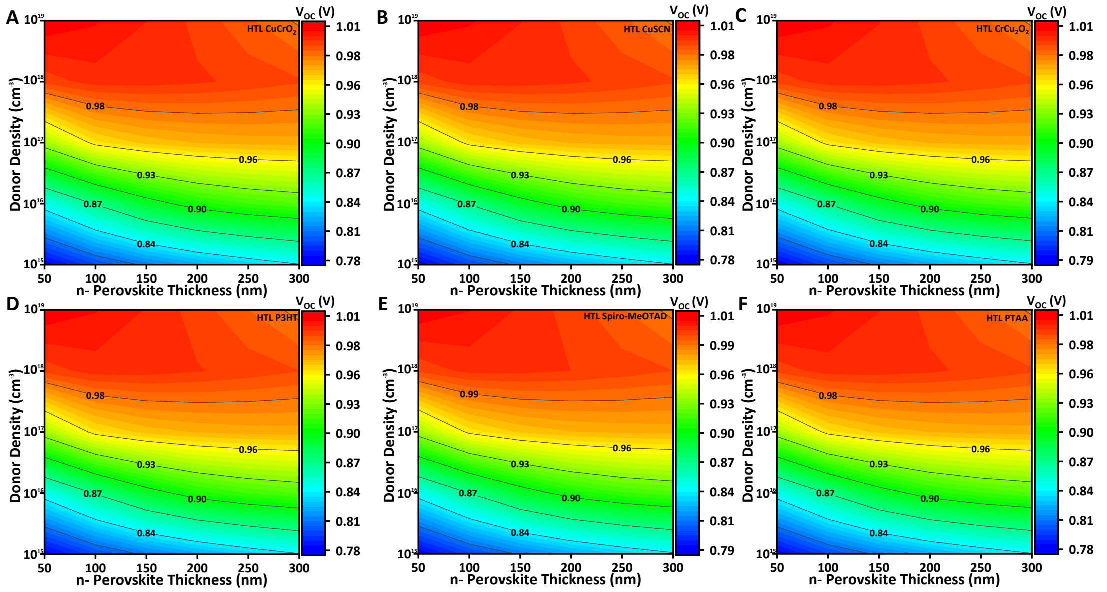

Figure S14. Contour plots demonstrate the simultaneous influence of varying n- perovskite thickness and N_D on V_{OC} for $FA_{0.75}MA_{0.25}Sn_{0.95}Ge_{0.05}I_3$-based PSCs when employing different HTLs; A) $CuCrO_2$, B) CuSCN, C) $SrCu_2O_2$, D) P3HT, E) Spiro-MeOTAD, and F) PTAA.

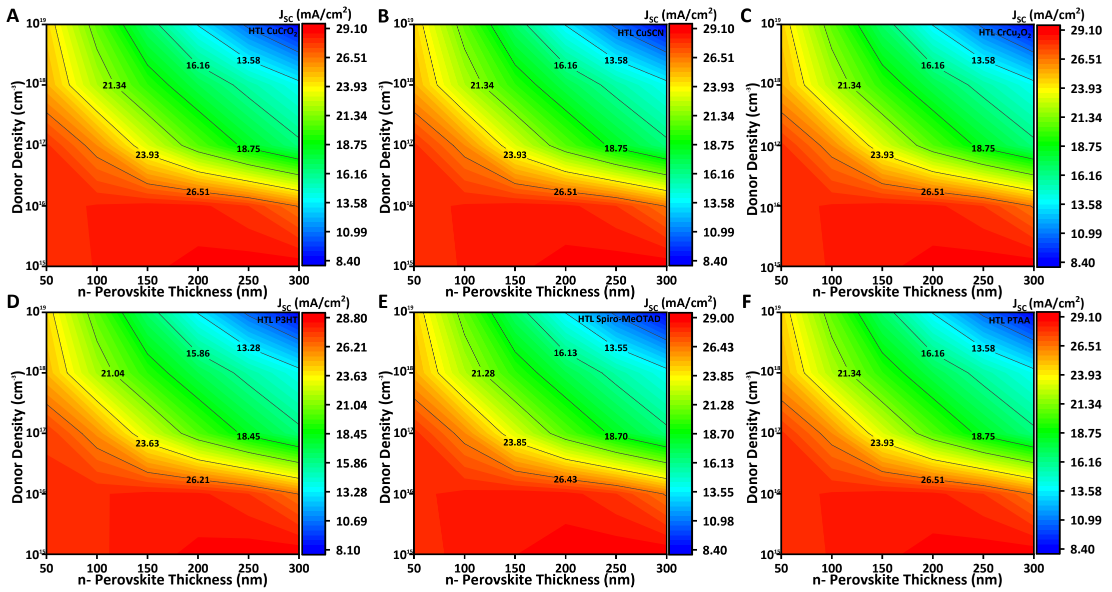

Figure S15. Contour plots demonstrate the simultaneous influence of varying n- perovskite thickness and N_D on J_{SC} for $FA_{0.75}MA_{0.25}Sn_{0.95}Ge_{0.05}I_3$-based PSCs when employing different HTLs; A) $CuCrO_2$, B) CuSCN, C) $SrCu_2O_2$, D) P3HT, E) Spiro-MeOTAD, and F) PTAA.

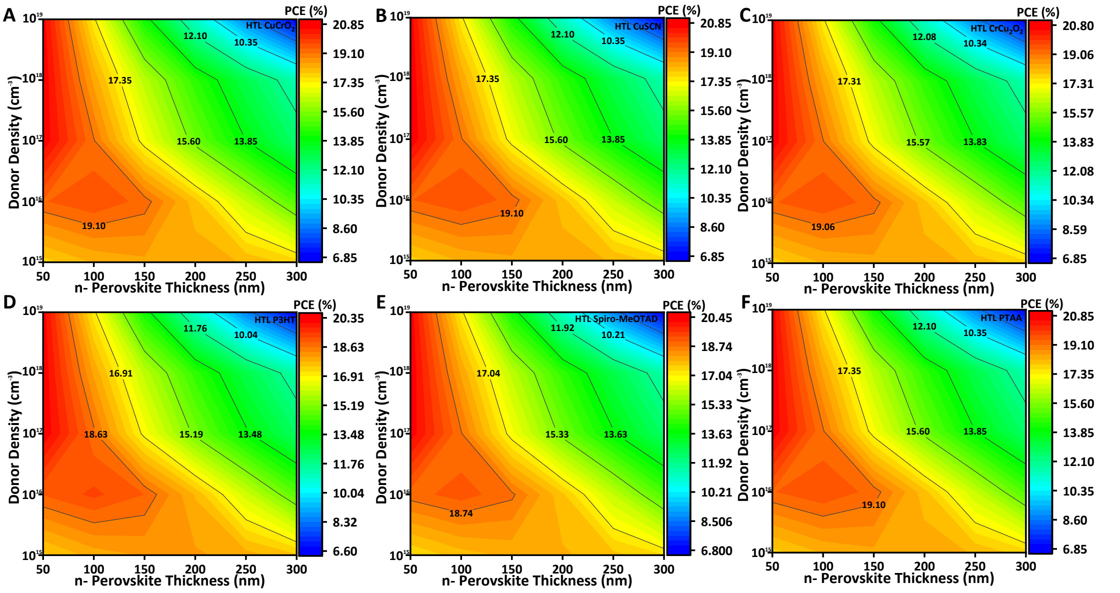

Figure S16. Contour plots demonstrate the simultaneous influence of varying n- perovskite thickness and N_D on PCE for $FA_{0.75}MA_{0.25}Sn_{0.95}Ge_{0.05}I_3$-based PSCs when employing different HTLs; A) $CuCrO_2$, B) CuSCN, C) $SrCu_2O_2$, D) P3HT, E) Spiro-MeOTAD, and F) PTAA.

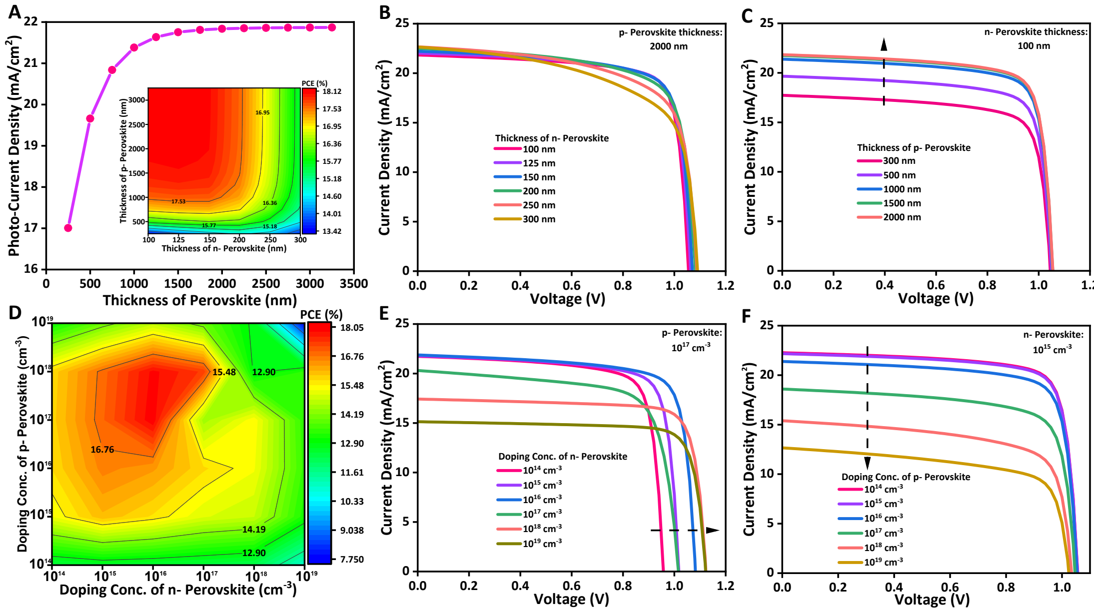

Figure S17. A) the effect of p- perovskite thickness on photo-current density and PCE contour of PSCs for varying n-perovskite and p-perovskite thicknesses and PCE contour of PSCs for varying n-perovskite and p-perovskite thicknesses, B) varying n-perovskite thicknesses J-V curve, C) varying p-perovskite thicknesses J-V curve, D) Contour plot displaying PCE values of PSCs based on diverse n- perovskite donor concentration and p- perovskie acceptor concentration, accompanied by corresponding J–V curves for E) n- perovskite and F) p- perovskite.

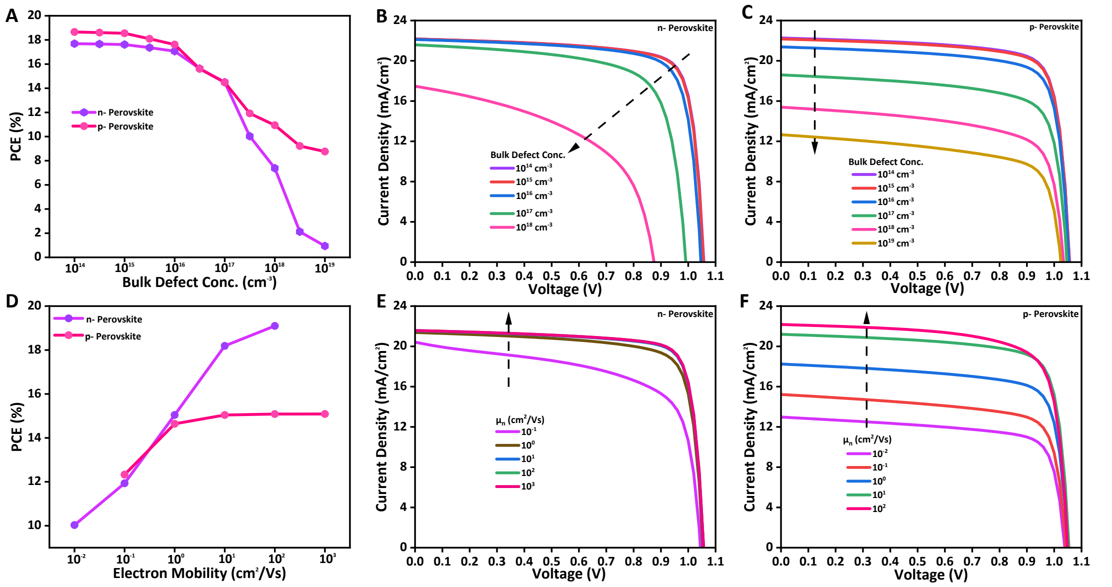

Figure S18. A) The influence of device performance on both p-type perovskite and n-type perovskite, B) Variations in bulk defect density in n-type perovskite and the resulting impact on J-V curves, C) Variations in bulk defect density in p-type perovskite and the consequent effect on J-V curves, D) The impact of mobility (μ_n) on the performance of both n-type and p-type perovskite devices, along with the respective J-V curves, E) Different values of µn for n-type perovskite and their effects on J-V curves, F) Different values of µn for p-type Perovskite and their effects on J-V curves.

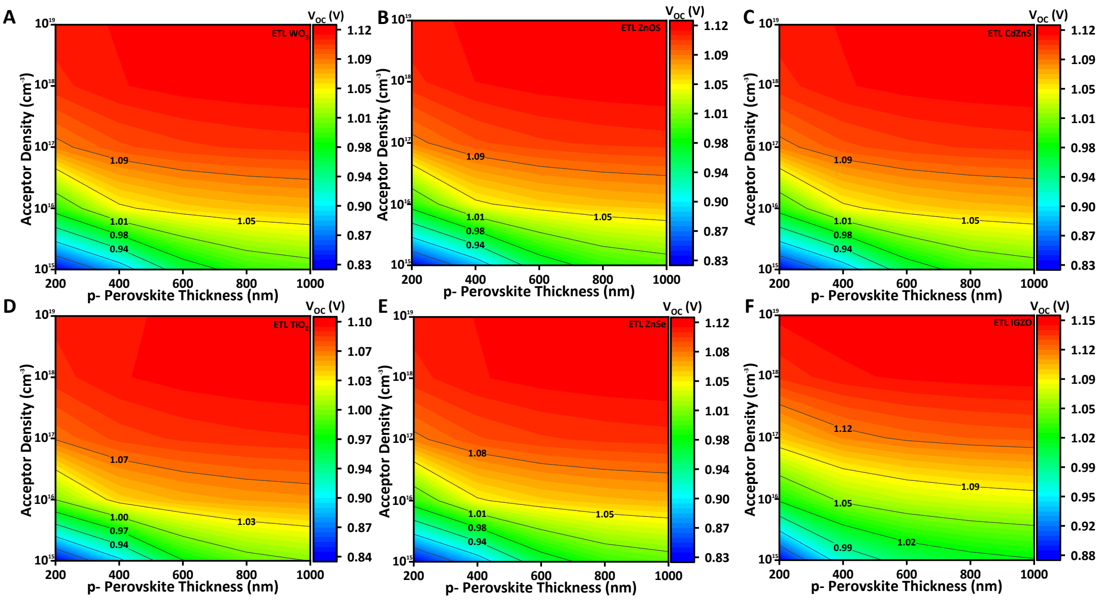

Figure S19. Contour plots demonstrate the simultaneous influence of varying p- perovskite thickness and N_A on V_{OC} for $MAPbI_3$-based PSCs when employing different ETLs; A) WO_3, B) ZnOS, C) CdZnS, D) TiO_2, E) ZnSe, and F) IGZO.

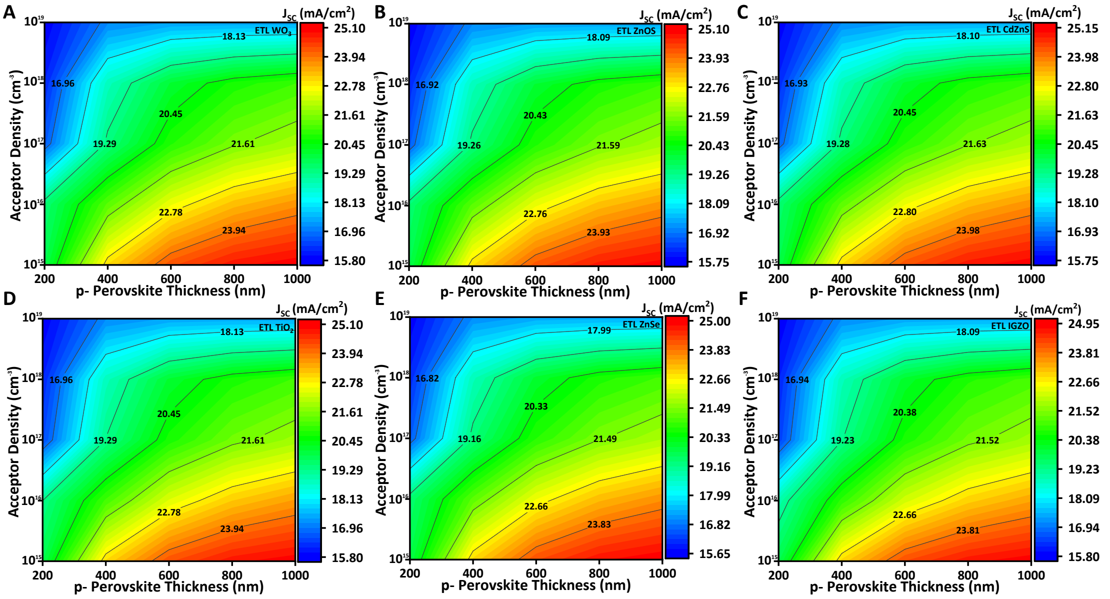

Figure S20. Contour plots demonstrate the simultaneous influence of varying p- perovskite thickness and N_A on J_{SC} for $MAPbI_3$-based PSCs when employing different ETLs; A) WO_3, B) ZnOS, C) CdZnS, D) TiO_2, E) ZnSe, and F) IGZO.

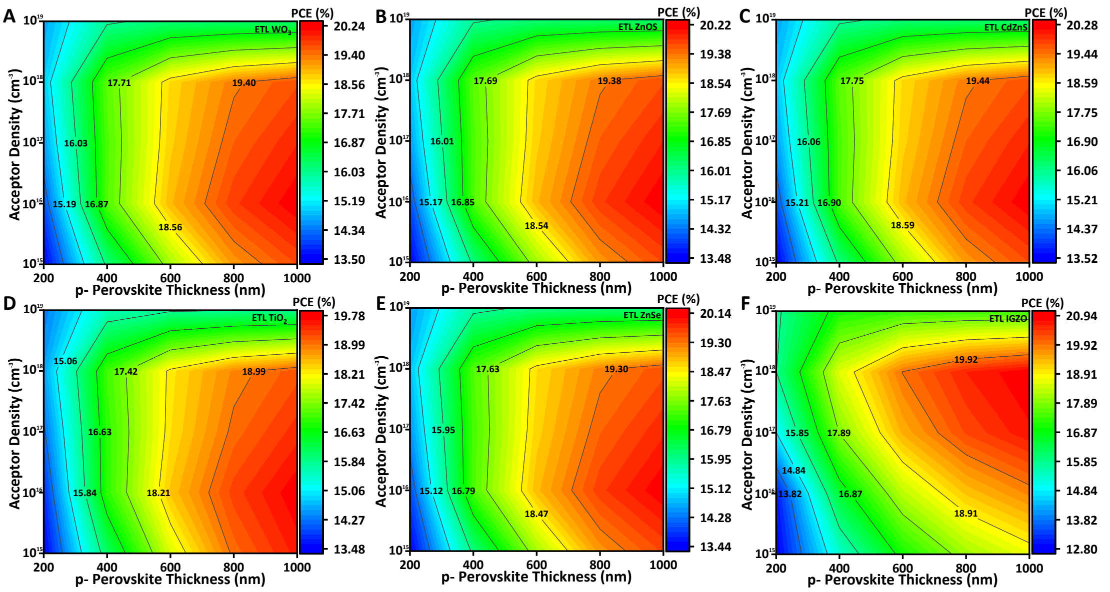

Figure S21. Contour plots demonstrate the simultaneous influence of varying p- perovskite thickness and N_A on PCE for $MAPbI_3$-based PSCs when employing different ETLs; A) WO_3, B) ZnOS, C) CdZnS, D) TiO_2, E) ZnSe, and F) IGZO.

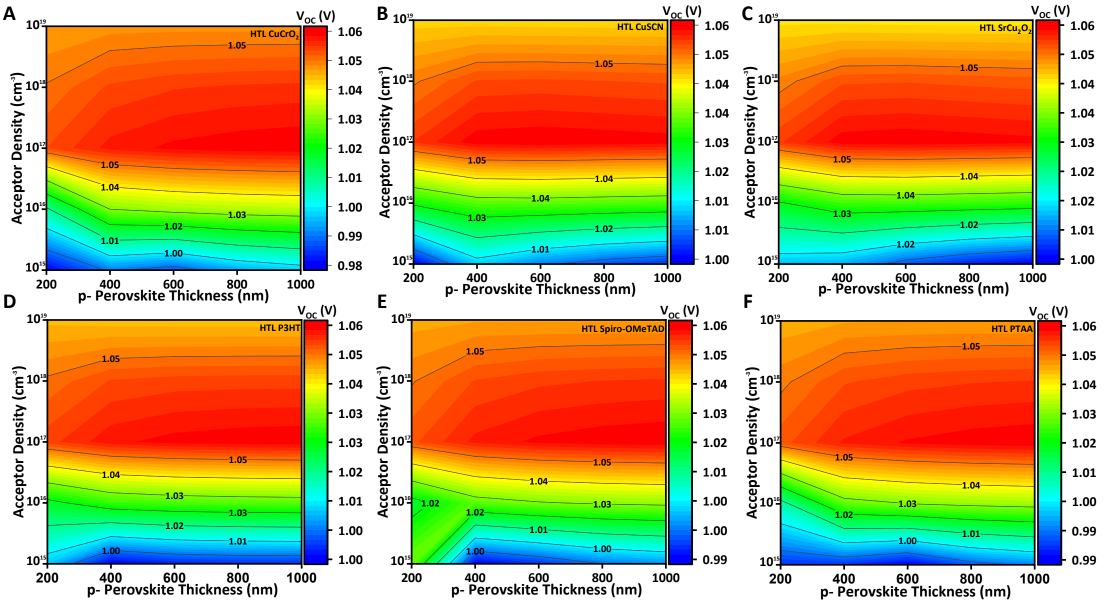

Figure S22. Contour plots demonstrate the simultaneous influence of varying p- perovskite thickness and N_A on V_{OC} for $MAPbI_3$-based PSCs when employing different HTLs; A) $CuCrO_2$, B) CuSCN, C) $SrCu_2O_2$, D) P3HT, E) Spiro-MeOTAD, and F) PTAA.

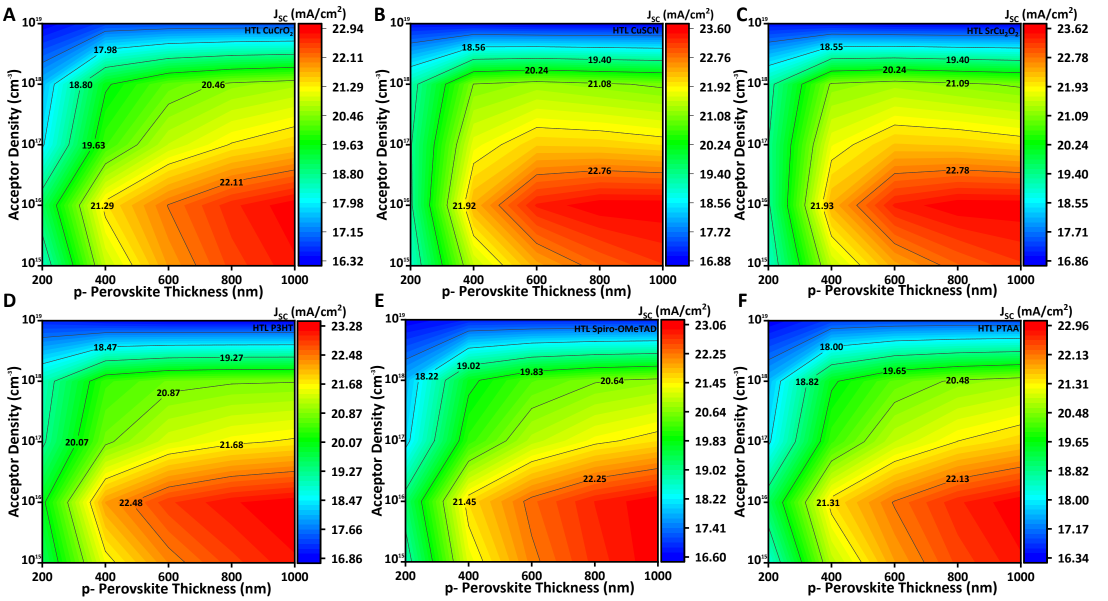

Figure S23. Contour plots demonstrate the simultaneous influence of varying p- perovskite thickness and N_A on J_{SC} for $MAPbI_3$-based PSCs when employing different HTLs; A) $CuCrO_2$, B) CuSCN, C) $SrCu_2O_2$, D) P3HT, E) Spiro-MeOTAD, and F) PTAA.

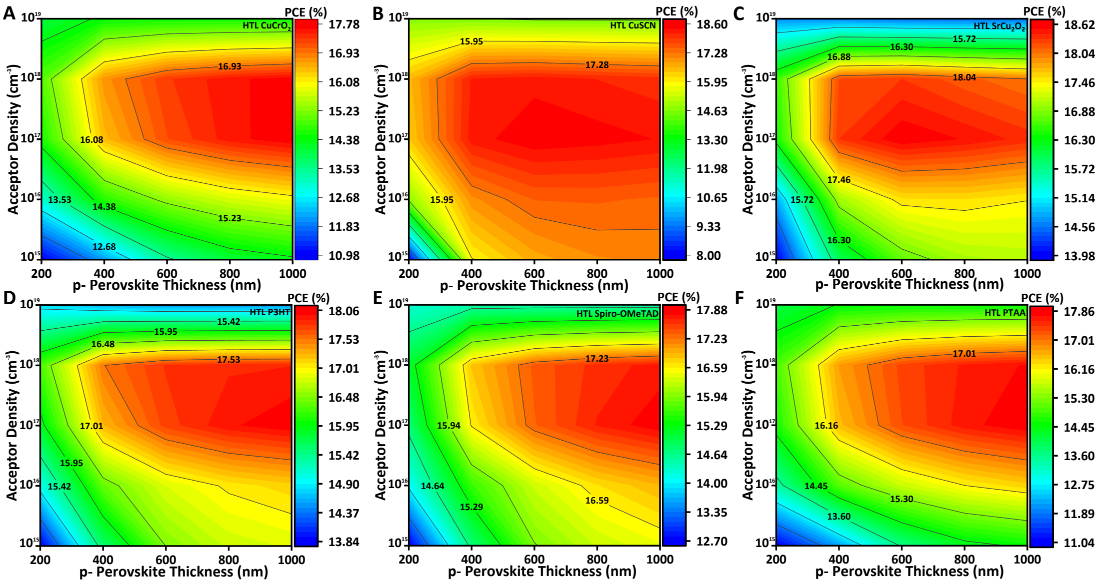

Figure S24. Contour plots demonstrate the simultaneous influence of varying p- perovskite thickness and N_A on PCE for $MAPbI_3$-based PSCs when employing different HTLs; A) $CuCrO_2$, B) CuSCN, C) $SrCu_2O_2$, D) P3HT, E) Spiro-MeOTAD, and F) PTAA.

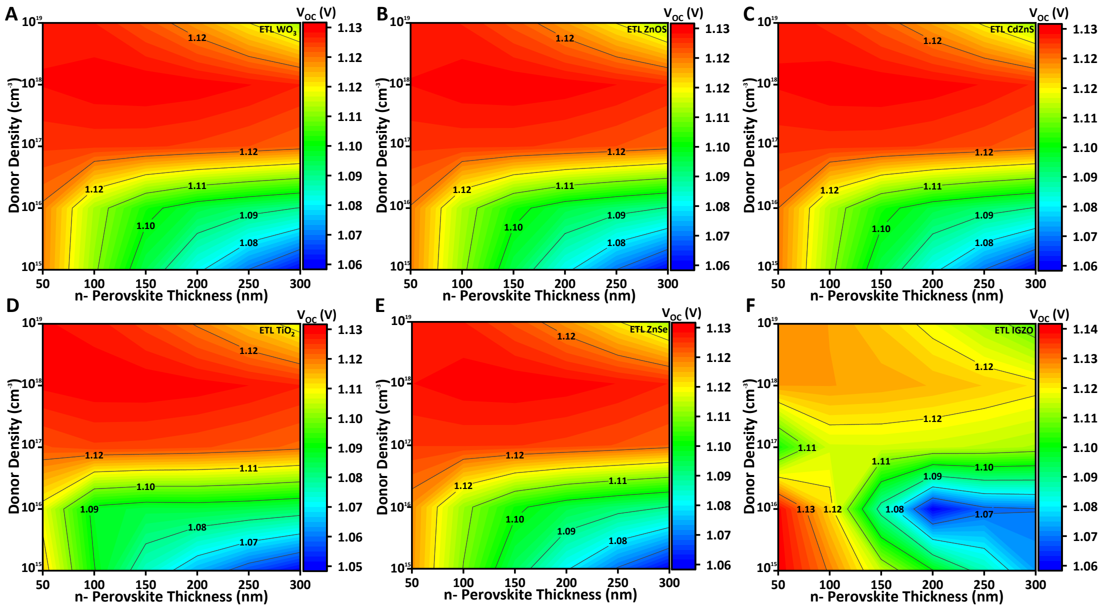

Figure S25. Contour plots demonstrate the simultaneous influence of varying n- perovskite thickness and N_D on V_{OC} for $MAPbI_3$-based PSCs when employing different ETLs; A) WO_3, B) ZnOS, C) CdZnS, D) TiO_2, E) ZnSe, and F) IGZO.

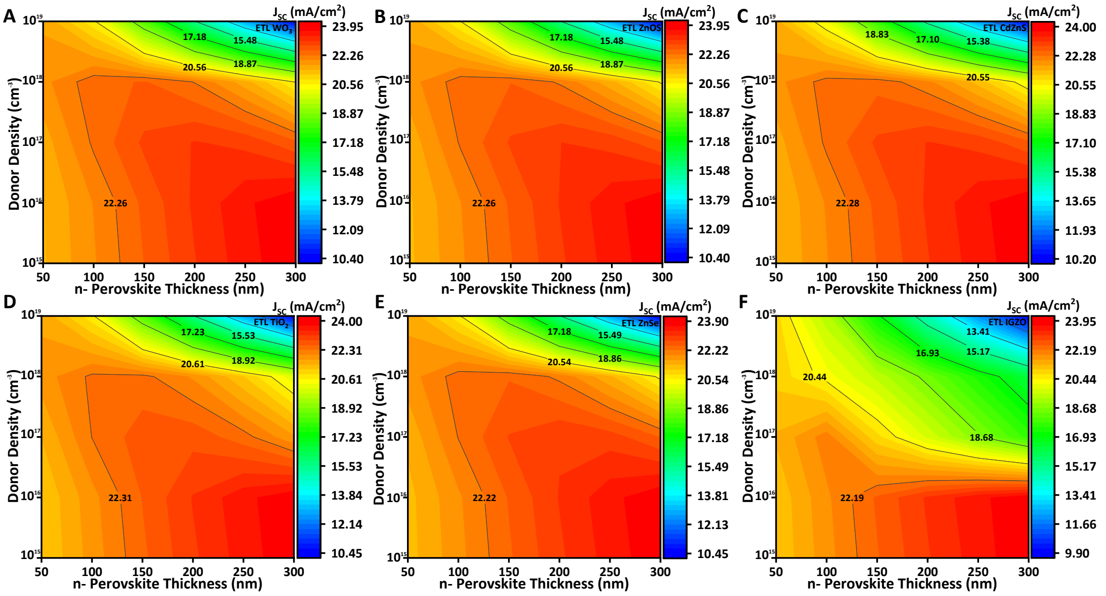

Figure S26. Contour plots demonstrate the simultaneous influence of varying n- perovskite thickness and N_D on J_{SC} for $MAPbI_3$-based PSCs when employing different ETLs; A) WO_3, B) ZnOS, C) CdZnS, D) TiO_2, E) ZnSe, and F) IGZO.

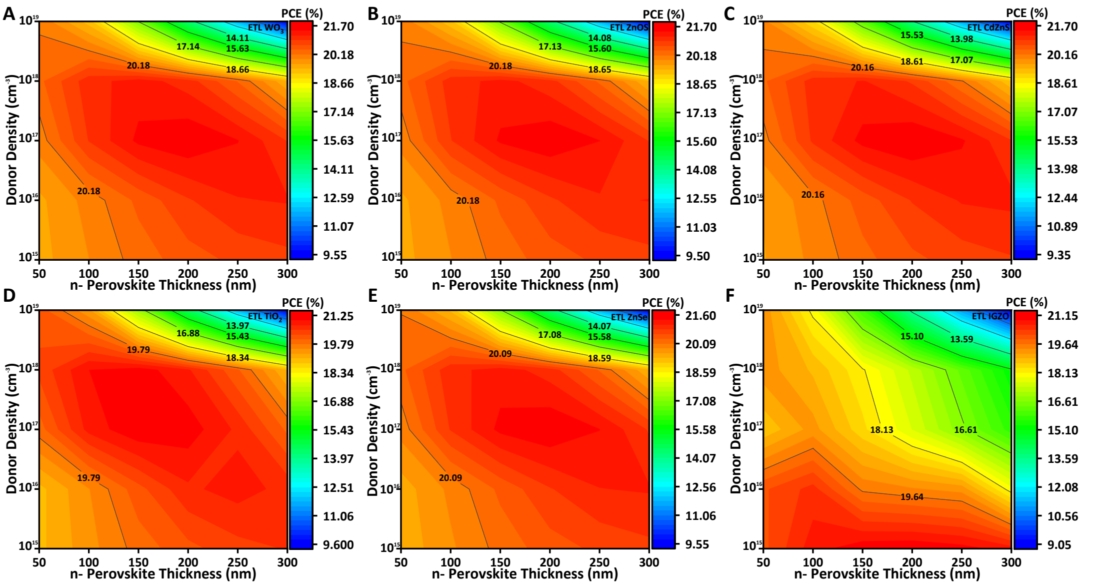

Figure S27. Contour plots demonstrate the simultaneous influence of varying n- perovskite thickness and N_D on PCE for $MAPbI_3$-based PSCs when employing different ETLs; A) WO_3, B) ZnOS, C) CdZnS, D) TiO_2, E) ZnSe, and F) IGZO.

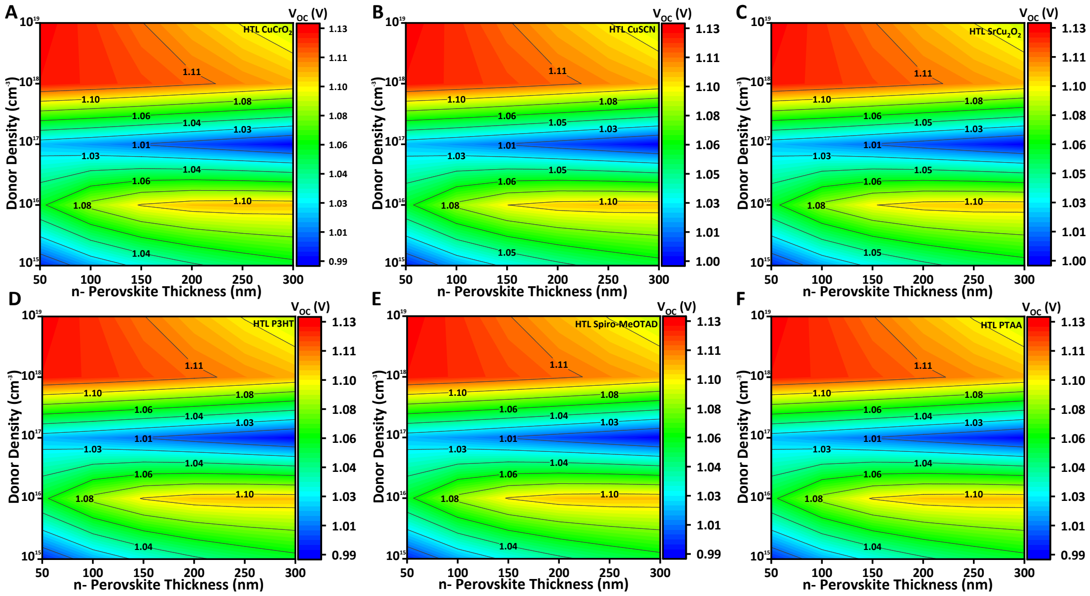

Figure S28. Contour plots demonstrate the simultaneous influence of varying n- perovskite thickness and N_D on V_{OC} for $MAPbI_3$-based PSCs when employing different HTLs; A) $CuCrO_2$, B) CuSCN, C) $SrCu_2O_2$, D) P3HT, E) Spiro-MeOTAD, and F) PTAA.

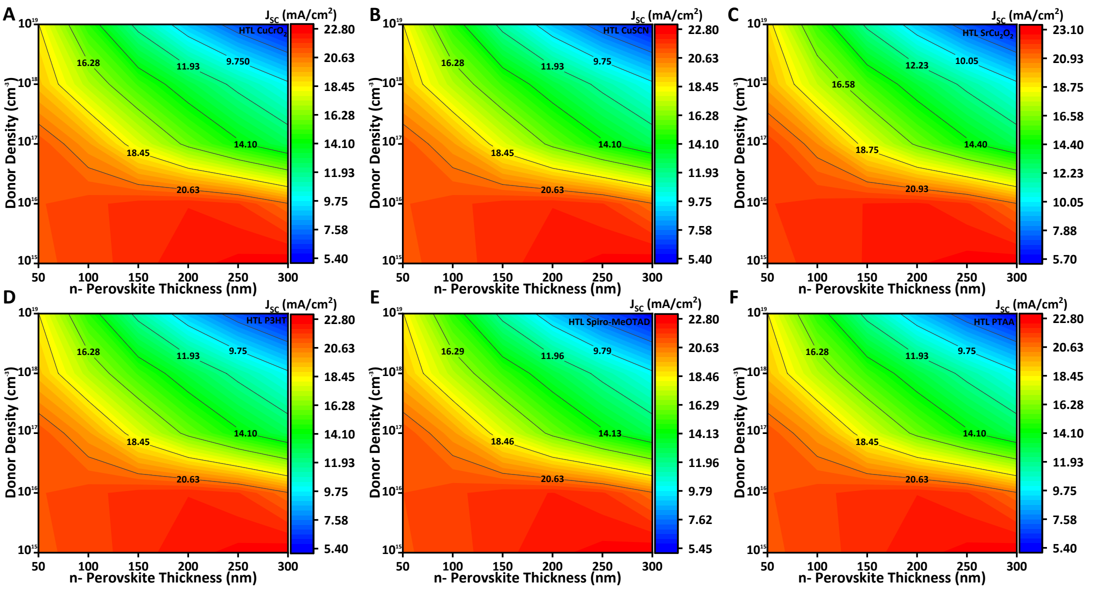

Figure S29. Contour plots demonstrate the simultaneous influence of varying n- perovskite thickness and N_D on J_{SC} for $MAPbI_3$-based PSCs when employing different HTLs; A) $CuCrO_2$, B) CuSCN, C) $SrCu_2O_2$, D) P3HT, E) Spiro-MeOTAD, and F) PTAA.

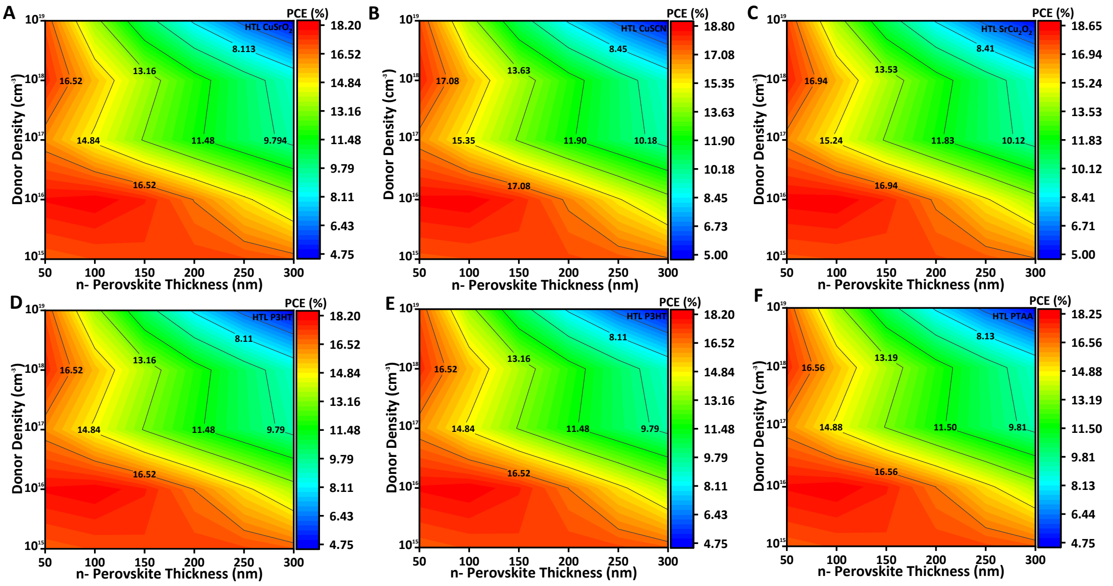

Figure S30. Contour plots demonstrate the simultaneous influence of varying n- perovskite thickness and N_D on PCE for $MAPbI_3$-based PSCs when employing different HTLs; A) $CuCrO_2$, B) CuSCN, C) $SrCu_2O_2$, D) P3HT, E) Spiro-MeOTAD, and F) PTAA.

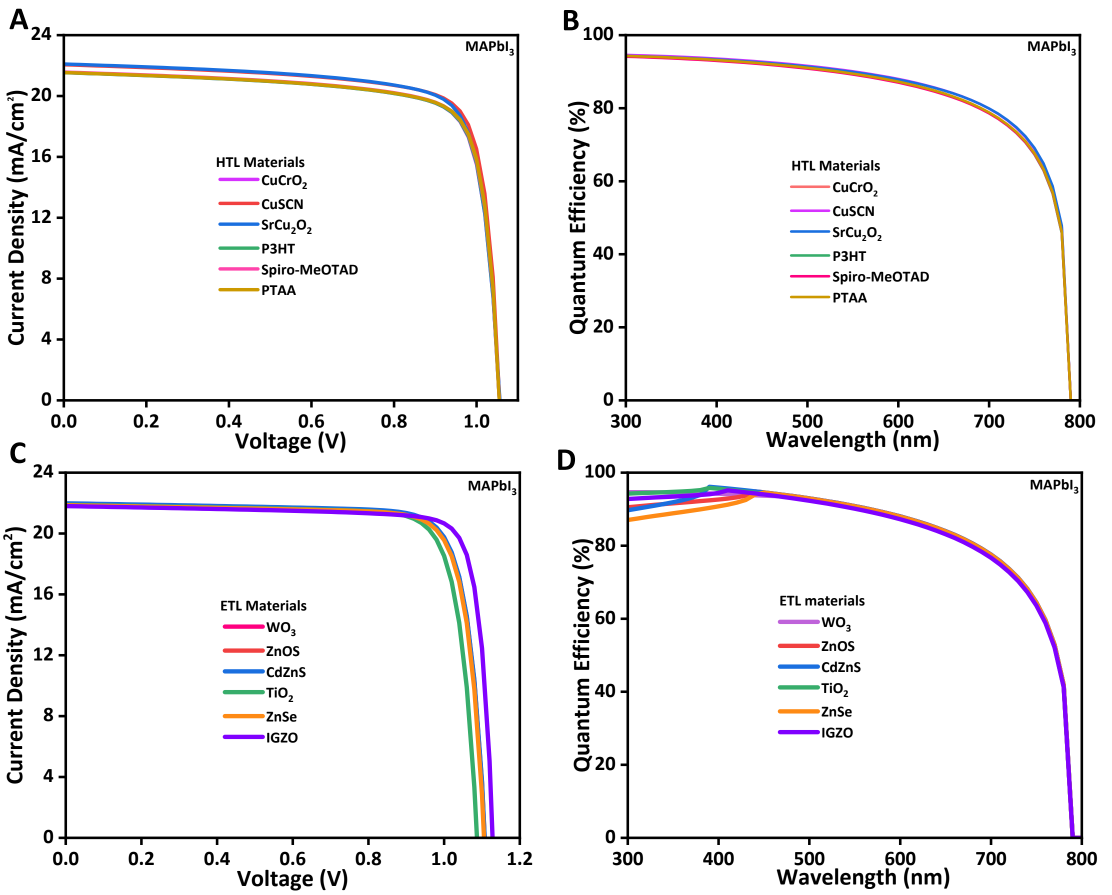

Figure S31. A) J-V Characteristics of $MAPbI_3$-Based solar cells with Various HTL, B) QE of the $MAPbI_3$-Based Solar Cells with Various HTL, C) J-V Characteristics of $MAPbI_3$-Based solar cells with Various ETL, D) QE of the $MAPbI_3$-Based Solar Cells with Various ETL.

Table S3- Performance properties for various HTL materials.

	FAMASnGeI$_3$				MAPbI$_3$			
HTL materials	V_{OC} (V)	J_{SC} (mA/cm^2)	FF (%)	PCE (%)	V_{OC} (V)	J_{SC} (mA/cm^2)	FF (%)	PCE (%)
$CuCrO_2$	0.95	26.08	76.48	19.13	1.05	21.53	78.16	17.77
CuSCN	0.95	26.09	76.49	19.14	1.05	22.05	78.83	18.37
$SrCu_2O_2$	0.95	26.08	76.26	19.08	1.05	22.10	77.97	18.22
P3HT	0.95	26.23	76.15	19.09	1.05	21.53	78.27	17.79
Spiro-MeOTAD	0.95	26.09	76.40	19.12	1.05	21.57	78.42	17.86
PTAA	0.95	26.08	76.48	19.14	1.05	21.54	78.53	17.84

Table S4- Performance properties for various ETL materials.

	FAMASnGeI$_3$				MAPbI$_3$			
ETL materials	V_{OC} (V)	J_{SC} (mA/cm^2)	FF (%)	PCE (%)	V_{OC} (V)	J_{SC} (mA/cm^2)	FF (%)	PCE (%)
WO_3	1.01	28.33	84.48	24.28	1.10	21.95	82.05	19.95
ZnOS	1.01	28.59	84.52	24.52	1.10	21.93	82.06	19.94
CdZnS	1.01	28.64	84.52	24.57	1.10	21.98	82.06	19.99
ZnSe	1.01	28.24	83.06	23.70	1.10	21.85	82	19.82
CdS	1	27.55	82.31	22.89	--	--	--	--
TiO_2	1.01	28.64	82.70	23.94	1.08	21.88	81.75	19.46
IGZO	--	--	--	--	1.12	21.80	84.24	20.73

References

1. Ravidas, B.K., M.K. Roy, and D.P. Samajdar. *Photovoltaic Performance Metrics of CsSnI3 Perovskite Solar Cells using SCAPS-1D*. in *2022 IEEE 6th Conference on Information and Communication Technology (CICT)*. 2022.
2. Zhang, Y., et al., *A Theoretical Investigation of Transport Layer-Free Homojunction Perovskite Solar Cells via a Detailed Photoelectric Simulation.* Advanced Energy Materials, 2023. **13**(12): p. 2203366.
3. Hossain, M.K., et al., *Photovoltaic performance investigation of Cs3Bi2I9-based perovskite solar cells with various charge transport channels using DFT and SCAPS-1D frameworks.* Energy & Fuels, 2023. **37**(10): p. 7380-7400.
4. Noman, M., et al., *26.48% efficient and stable FAPbI 3 perovskite solar cells employing SrCu 2 O 2 as hole transport layer.* RSC advances, 2023. **13**(3): p. 1892-1905.
5. Shasti, M. and A. Mortezaali, *Numerical study of Cu2O, SrCu2O2, and CuAlO2 as hole-transport materials for application in perovskite solar cells.* physica status solidi (a), 2019. **216**(18): p. 1900337.
6. Sarkar, D.K., et al., *A comprehensive study on RbGeI3 based inorganic perovskite solar cell using green synthesized CuCrO2 as hole conductor.* Journal of Photochemistry and Photobiology A: Chemistry, 2023. **439**: p. 114623.
7. Karthick, S., et al., *Efficient 2T C s KP b (IB r) 3—Tin Incorporated Narrow Bandgap Perovskite Tandem Solar Cells: A Numerical Study with Current Matching Conditions.* Advanced Theory and Simulations, 2021. **4**(11): p. 2100121.
8. Hossain, M.K., et al., *Design and Simulation of Cs2BiAgI6 Double Perovskite Solar Cells with*

Different Electron Transport Layers for Efficiency Enhancement. Energy & Fuels, 2023. **37**(5): p. 3957-3979.

9. Hossain, M.K., et al., *An extensive study on multiple ETL and HTL layers to design and simulation of high-performance lead-free CsSnCl3-based perovskite solar cells.* Scientific Reports, 2023. **13**(1): p. 2521.
10. Rahman, M.B., et al., *Selection of a compatible electron transport layer and hole transport layer for the mixed perovskite FA 0.85 Cs 0.15 Pb (I 0.85 Br 0.15) 3, towards achieving novel structure and high-efficiency perovskite solar cells: a detailed numerical study by SCAPS-1D.* RSC advances, 2023. **13**(25): p. 17130-17142.
11. Bhavsar, K. and P. Lapsiwala, *Numerical simulation of perovskite solar cell with different material as electron transport layer using SCAPS-1D Software.* Semicond. Phys. Quantum Electron. Optoelectron, 2021. **24**: p. 341-347.
12. Ijaz, S., et al., *Numerical simulation to optimize the efficiency of HTM-free perovskite solar cells by ETM engineering.* Solar Energy, 2023. **250**: p. 108-118.